An efficient second-order linear scheme for the phase field model of corrosive dissolution

Huadong Gao[a], Lili Ju[b,*], Ravindra Duddu[c], Hongwei Li[d]

[a]*School of Mathematics and Statistics & Hubei Key Laboratory of Engineering Modeling and Scientific Computing, Huazhong University of Science and Technology, Wuhan, Hubei 430074, China.*
[b]*Department of Mathematics, University of South Carolina, Columbia, SC 29208, USA.*
[c]*Department of Civil and Environmental Engineering, Vanderbilt University, Nashville, TN 37205, USA.*
[d]*School of Mathematics and Statistics, Shandong Normal University, Jinan, Shandong 250014, China.*

Abstract

In this paper we propose an efficient numerical scheme for solving the phase field model (PFM) of corrosive dissolution that is linear and second-order accurate in both time and space. The PFM of corrosion is based on the gradient flow of a free energy functional depending on a phase field variable and a single concentration variable. While classic backward differentiation formula (BDF) schemes have been used for time discretization in the literature, they require very small time step sizes owing to the strong numerical stiffness and nonlinearity of the parabolic partial differential equation (PDE) system defining the PFM. Based on the observation that the governing equation corresponding to the phase field variable is very stiff due to the reaction term, the key idea of this paper is to employ an exponential time integrator that is more effective for stiff dynamic PDEs. By combining the exponential integrator based Rosenbrock–Euler scheme with the classic Crank–Nicolson scheme for temporal integration of the spatially semi-discretized system, we develop a decoupled linear numerical scheme that alleviates the time step size restriction due to high stiffness. Several numerical examples are presented to demonstrate accuracy, efficiency and robustness of the proposed scheme in two-dimensions, and we find that a time step size of 10^{-3} second for meshes with the typical spatial resolution 1 μm is stable. Additionally, the proposed scheme is robust and does not suffer from any convergence issues often encountered by nonlinear Newton methods.

Keywords: Corrosive dissolution, pitting corrosion, phase field model, exponential integrator, numerical stiffness, semi-implicit scheme

---

1. Introduction

Localized corrosion of stainless steel and aluminum alloys, including pitting and crevice corrosion, stress corrosion cracking and corrosion fatigue, poses a significant threat to the safety of aerospace, civil and transportation infrastructure. Corrosion pits and crevices cause stress concentrations and promote the nucleation of fatigue cracks [21, 43], which are often difficult to detect before a structure or its component fails. Mathematical and computational modeling of localized corrosion phenomena is necessary not only to

---

[*] Corresponding author

Email addresses: `huadong@hust.edu.cn` (Huadong Gao), `ju@math.sc.edu` (Lili Ju), `ravindra.duddu@vanderbilt.edu` (Ravindra Duddu), `hwli@sdnu.edu.cn` (Hongwei Li)

gain a better understanding of the complex physical and chemical mechanisms, but also to enable more reliable and robust prediction of corrosion damage evolution in structures. Recently, the phase field modeling approach has been utilized to predict the spatial-temporal evolution of the corrosion damage [e.g., 1, 32]. The main advantage of the phase field model (PFM) is that it describes the evolution of interfaces without explicitly tracking the interface within a finite element or finite difference implementation. However, a major limitation of the PFM is the computational expense associated with simulating corrosion pit/crevice evolution over long times and larger spatial domains, despite the availability of high performance computing platforms. Therefore, in this paper we develop an efficient numerical scheme for solving the phase field equations governing diffusion-controlled corrosive dissolution.

Localized corrosion involves the rapid dissolution of a passive metal/alloy in a corrosive environment at discrete sites where the protective passive film has broken down [12]. The initiation or nucleation process involving passive film breakdown is stochastic in nature and takes place on smaller length scales (on the order of nanometers), so it is not possible to predict exactly when and where pits will nucleate. Broadly, there are two classes of models for predicting corrosion damage evolution: purely empirical and mechanistic/deterministic. Purely empirical models, including statistical or probabilistic, and artificial neural networks models [31, 37], need large databases for calibration. However, due to the scarcity of data on failure events, it is difficult to construct well-calibrated empirical models, so their predictive capability is generally limited [30, 48]. Mechanistic/deterministic models consider the physical and chemical processes of corrosion propagation after initiation based on mass, charge and/or momentum balance. In this paper, we restrict our attention to mechanistic modeling of localized corrosion that considers the anodic dissolution of metal (electrode) as metal ions at discrete initiation sites into an aqueous solution environment (electrolyte). Thus, localized corrosive dissolution is defined by a moving interface problem, with the evolution of the corrosion interface and the chemistry of the solution environment governed by coupled nonlinear partial differential equations (PDEs). The complexity of this moving interface problem along with the vast separation of timescales between electrode interface evolution (i.e., corrosion) and ion diffusion in the electrolyte (i.e., transport) poses significant computational challenges, which necessitates the development of robust and efficient numerical methods.

Moving interfaces or free boundaries are ubiquitous in multi-component and multi-phase material systems and modeling their complex topology and evolution patterns is important to a wide range of engineering and scientific disciplines. Several computational models have been developed for solving moving interface or free boundary problems, which can be broadly classified as either sharp-interface or diffuse-interface models. The sharp-interface models assume that the interface thickness is negligible (zero), and they can be implemented using both fixed or moving grid/mesh methods. Several sharp-interface corrosion models have been proposed that use the finite element method to solve the governing equations [9, 10, 27, 41, 45, 47, 53, 55]. The moving sharp-interface was treated in [27, 41, 45, 47, 53, 55] using remeshing or mesh moving or arbitrary Lagrangian–Eulerian methods, which can be computationally expensive and cumbersome. Alternatively, in [9, 10] the combined extended finite element and level set method was employed to capture the evolution of the sharp-interface without remeshing; however, it is currently not well developed in three dimensions. On the other hand, the diffuse-interface models assume that the interface thickness is small, but finite, and are usually implemented using fixed grid/mesh methods. Several diffuse-interface corrosion models have been proposed, including cellular automation models [40], finite volume models [42], peridynamic models [7, 8], and phase field models (PFM) [1, 32–34]. While PFMs have only been recently used to study corrosion, they have been extensively used to study a variety of moving interface problems, such as solidification [4, 24], microstructure evolution [6], thin film evolution [39], superconductivity [13], and dendrite growth [50, 51].

In this paper, we consider a simplified PFM for simulating pitting corrosion presented in [32] using the free energy density function developed in [25]. This PFM coupling the Allen–Cahn and Cahn–Hilliard equations can be viewed as a gradient flow problem of a free energy functional consisting of a phase field variable ϕ (non-conserved) and a concentration variable c (conserved), respectively. The model parameters are calibrated in [32] by matching the corrosion rate with that from a sharp-interface model [9]. Thus, the model is described by a system of two coupled parabolic PDEs (see Section 2 for details); however, the main numerical challenge arises from the strong stiffness and nonlinearity of this parabolic system of equations, which severely restricts the time step size. To illustrate this, we introduce all the model parameter values (see Table 4) into the governing equations (2.11)–(2.12) to obtain the following PDE system:

$$\begin{cases} \dfrac{\partial \phi}{\partial t} = 6.01 \times 10^{-6} \Delta \phi - 4.16 \times 10^{6} g'(\phi) + 2.06 \times 10^{8} (c - 0.04 - 0.96 h(\phi)) h'(\phi), & (1.1) \\ \dfrac{\partial c}{\partial t} = 8.50 \times 10^{-10} \Delta c - 8.50 \times 10^{-10} \Delta (0.96 h(\phi) + 0.04), & (1.2) \end{cases}$$

where $h(\phi) = -2\phi^3 + 3\phi^2$ and $g(\phi) = \phi^2(1-\phi)^2$, and up to three significant digits are shown for each coefficient. Note that the range for the values of ϕ and c is $[0, 1]$. It is evident that the coefficients of the reaction and diffusion terms in (1.2) are of the same order magnitude $O(10^{-10})$; whereas, the coefficient of the reaction term in (1.1) for ϕ is of the order $O(10^{8})$, but the coefficient of the diffusion term is very small, $O(10^{-6})$. Consequently, equation (1.1) is extremely stiff with respect to ϕ and an extremely small time step size is needed if conventional backward differentiation formula (BDF) schemes are used for the temporal discretization. For example, in [32] an adaptive, second-order accurate BDF2 scheme was used along with the standard finite element approximation and a nonlinear solver to solve the above PFM for pitting corrosion. Although adaptive time-stepping strategy was used in [32], a very small time step size $\tau = 10^{-8}$ second on adaptively refined spatial meshes with a typical resolution of 1 μm in the vicinity of the interface may be necessary at the beginning stages of the simulations. It is noteworthy that such a small time step size (much smaller than that required for accuracy) may be necessary to alleviate spurious oscillations in the field variables or convergence issues with the nonlinear solver for the PFM.

To overcome this severe time step restriction due to the numerical stiffness of (1.1), we resort to exponential time-integrator or exponential time-differencing schemes, which were first used successfully in chemical physics [36, 38]. The applications of exponential time-integrators were originally limited by the computational difficulty/expense associated with the product of a matrix exponential with a vector, which is particularly challenging if the dimension of the matrix is large. Since then tremendous efforts have been devoted to the development of efficient time-integrators and significant progress has been made [e.g., 2, 3, 16–18, 49]. More recently, exponential integrator based methods have been used to solve: Navier–Stokes equations [23, 29], shallow water equations [14], porous media flow [46] and grain coarsening in crystalline materials [22, 56]. A major advantage of the exponential integrators is their robustness and effectiveness in dealing with stiff evolution problems, see the discussion in [19, 20]. In view of practical implementation, there are several efficient packages for computing the action of the exponential of a matrix on the operand vector, for instance, the package `Expokit` by Sidje [44], `expmv` by Al-Mohy and Higham [3] and `KIOPS` by Gaudreault, Rainwater and Tokman [15]. Inspired by the above mentioned studies, in this paper we apply the exponential integrator to solve equation (1.1) for the phase field variable ϕ. Moreover, by noting that the diffusion and the reaction coefficients are of the same order in equation (1.2) for the concentration variable c, we use the standard Crank–Nicolson scheme. Furthermore, we decouple the parabolic PDE system and successfully develop an efficient linear, second-order accurate scheme. This scheme alleviates the severe restriction on time step size τ as demonstrated by numerical benchmark tests.

The rest of this paper is organized as follows: In Section 2, we provide a brief description of the phase field model for corrosive dissolution. In Section 3, we present a decoupled linear numerical scheme for solving the governing equations of the model, where the central finite difference is used for spatial discretization, and an exponential time integrator and the Crank–Nicolson scheme are used for temporal discretization. We also perform local truncation error analysis to show the second-order accuracy of the proposed numerical scheme in time and space. In Section 4, we present several numerical benchmark tests to demonstrate that the proposed scheme is efficient and accurate for simulating the morphological evolution of corrosion interface. Finally, in Section 5, we provide a brief summary and some concluding remarks.

2. Phase field model for corrosive dissolution

In this section, we give a brief description of the phase field model for corrosive dissolution, and for a more detailed discussion we refer the reader to [32]. This model is based on the phenomenologically oriented single-phase-field model for solidification [25, 35]. There are two variables in this model: (1) a phase field variable ϕ is introduced to represent the state of the material, such that $\phi = 1$ indicates the metal (solid) and $\phi = 0$ indicates the aqueous solution (liquid) domains, respectively; and (2) a normalized concentration variable c is introduced to describe the total metal ion concentration in solution, such that $0 \leq c \leq 1$. For example, for the 304 stainless steel (SS) alloy, the normalized concentration is defined as $c = \bar{c}/\bar{c}_{\text{solid}}$, where the variable $\bar{c}$ is the total molar concentration of Fe^{2+}, Cr^{3+}, and Ni^{2+} ions and the constant $\bar{c}_{\text{solid}}$ is the concentration of metal atoms in solid phase. The variable ϕ varies continuously across the narrow diffuse-interface of thickness l. For convenience, we list the nomenclature used in this paper in Table 1.

Table 1: Nomenclature.

Notation	Physical interpretation
A	Free energy density curvature
$\bar{c}$	Total molar concentration of metal ions or atoms
$\bar{c}_{\text{solid}}$	Molar concentration of the metal atoms in solid
$\bar{c}_{\text{sat}}$	Saturation concentration of metal ions in solution
c	Normalized molar concentration of metal ions or atoms
c_{Se}	Normalized equilibrium concentration in solid
c_{Le}	Normalized equilibrium concentration in solution
D	Diffusion coefficient
f	Local free energy density
f_{S}	Free energy density of the solid phase
f_{L}	Free energy density of the solution phase
f_{int}	Interface free energy density
$\mathcal{F}$	Free energy functional of the system
L	Interface kinetics coefficient
l	Interface thickness
M	Diffusion mobility
α_c	Concentration gradient energy coefficient
α_ϕ	Phase field variable gradient energy coefficient
ϕ	Phase field variable

The driving force for any phase transformation is the reduction of the total free energy $\mathcal{F}$ of the thermodynamic system. In this simplified PFM for corrosive dissolution [32], $\mathcal{F}$ consists of the homogeneous bulk or local free energy $\mathcal{F}_{\text{bulk}}$ and the interface energy $\mathcal{F}_{\text{int}}$ defined as

$$\mathcal{F}(\phi, c) = \mathcal{F}_{\text{bulk}} + \mathcal{F}_{\text{int}} = \int_{\Omega} \Big[f(\phi(\boldsymbol{x}, t), c(\boldsymbol{x}, t)) + f_{\text{int}}(\phi(\boldsymbol{x}, t), c(\boldsymbol{x}, t)) \Big] \, \mathrm{d}\boldsymbol{x}, \tag{2.1}$$

where Ω denotes the computational domain containing both the metal and solution phases, $\boldsymbol{x}$ denotes the spatial coordinates, t is the time, $f(\phi, c)$ is the local free energy density, and $f_{\text{int}}(\phi, c)$ is the surface energy density associated with the diffuse-interface, respectively. The surface energy is the excess energy at the surface that arises from the inhomogeneity within the interface region defined in terms of the field variable gradients as

$$f_{\text{int}}(\phi, c) = \frac{\alpha_\phi}{2}(\nabla\phi)^2 + \frac{\alpha_c}{2}(\nabla c)^2, \tag{2.2}$$

where α_ϕ and α_c are the gradient energy coefficients associated with the ϕ and c, respectively.

The local free energy density $f(\phi, c)$ refers to a homogeneous system, where all the field variables are constant in the domain (i.e., gradients are zero). There are many differences with the formulation of free energy functionals in PFMs depending upon the application (see [35] for detailed review). In our case, the function $f(\phi, c)$ comprises of an interpolation of free energy expressions of the coexisting solid f_S and liquid f_L phases and a double-well function $g(\phi)$ as

$$f(\phi, c) = h(\phi) f_S(c_S) + [1 - h(\phi)] f_L(c_L) + w g(\phi), \tag{2.3}$$

where $h(\phi) = -2\phi^3 + 3\phi^2$ is a C^∞-continuous interpolation function such that $h(0) = 0$ and $h(1) = 1$, and w is the height of the double well potential $g(\phi) = \phi^2(1 - \phi)^2$. It is assumed that the diffuse-interface is a mixture of the solid and liquid phases with different normalized concentrations c_S and c_L, respectively, but the chemical potential in both phases is the same, that is,

$$c = h(\phi) c_S + (1 - h(\phi)) c_L, \quad \frac{\partial f_S(c_S)}{\partial c_S} = \frac{\partial f_L(c_L)}{\partial c_L}. \tag{2.4}$$

The free energy density functions of the coexisting solid and liquid phases are approximated as

$$f_S(c_S) = A(c_S - c_{Se})^2, \quad f_L(c_L) = B(c_L - c_{Le})^2 \tag{2.5}$$

where $c_{Se} = \bar{c}_{\text{solid}}/\bar{c}_{\text{solid}} = 1$ and $c_{Le} = \bar{c}_{\text{sat}}/\bar{c}_{\text{solid}}$ are the normalized equilibrium concentrations for the solid and liquid phases, respectively. In (2.5), A and B are the free energy density curvatures of the solid and liquid phases. The curvatures are assumed to be the same for both the solid and liquid phases in this model, i.e., $A = B$ [32]. Combining (2.4) and (2.5), we can derive the final expression for the local free energy density as

$$f(\phi, c) = A\big(c - h(\phi)(c_{Se} - c_{Le}) - c_{Le}\big)^2 + w g(\phi)\,. \tag{2.6}$$

To assure the decrease of the free energy during the corrosion process, the governing phase field equations are derived by minimizing $\mathcal{F}$ via its gradient flow [32]:

$$\begin{cases} \dfrac{\partial \phi}{\partial t}(\mathbf{x}, t) = -L\dfrac{\delta \mathcal{F}}{\delta \phi} = -L\left(\dfrac{\partial f}{\partial \phi} - \alpha_\phi \nabla^2 \phi\right), & (2.7) \\ \dfrac{\partial c}{\partial t}(\mathbf{x}, t) = \nabla \cdot M\nabla\dfrac{\delta \mathcal{F}}{\delta c} = \nabla \cdot M\nabla\left(\dfrac{\partial f}{\partial c} - \alpha_c \nabla^2 c\right), & (2.8) \end{cases}$$

where L is the interface kinetics parameter and M is the diffusion mobility for mass transport. In practice, only one of the gradient terms (∇c or $\nabla\phi$) would be sufficient to approximate the energy contribution from the diffuse interface, thus the concentration gradient energy coefficient $\alpha_c = 0$ is often assumed. The gradient energy coefficient α_ϕ and the height of double well potential w are correlated to the interface energy σ and interface thickness l as

$$\sigma \approx \sqrt{16 w \alpha_\phi}, \quad l = \alpha^* \sqrt{\frac{2\alpha_\phi}{w}}, \tag{2.9}$$

where $\alpha^* = 2.94$ is a constant parameter. The diffusion mobility M can be defined as

$$M = \frac{D}{2A}, \tag{2.10}$$

where D is the Fick's diffusion coefficient. Thus, phase field equations (2.7)–(2.8) can be represented by the following parabolic partial differential equation system:

$$\begin{cases} \dfrac{\partial \phi}{\partial t} = -L\Big(2A(c_{Le} - c_{Se})[c - h(\phi)(c_{Se} - c_{Le}) - c_{Le}]h'(\phi) + wg'(\phi) - \alpha_\phi \Delta\phi\Big), & (2.11) \\ \dfrac{\partial c}{\partial t} - 2AM\Delta c = -2AM\Delta\Big(h(\phi)(c_{Se} - c_{Le}) + c_{Le}\Big) & (2.12) \end{cases}$$

together with appropriate Dirichlet and Neumann boundary and initial conditions.

3. A decoupled, second-order accurate linear numerical scheme

3.1. Spatial discretization

For simplicity, we first consider a rectangular domain $\Omega = [0, L_x] \times [0, L_y]$ in two dimensional space. A uniform $N_x \times N_y$ grid/mesh Ω_h is used with mesh size $\max\{h_x, h_y\}$ where $h_x = \frac{L_x}{N_x}$ and $h_y = \frac{L_y}{N_y}$. We denote the spatial coordinates of the grid nodes by $\{\boldsymbol{x}_{i,j}\}$ for $0 \le i \le N_x$ and $0 \le j \le N_y$. For a continuous function u defined on Ω, $U_h = \{u_{i,j}\}$ is its approximation defined on Ω_h with $u_{i,j} = u(\boldsymbol{x}_{i,j})$. The standard second-order central finite difference approximation for the Laplacian Δu at $\boldsymbol{x}_{i,j}$ is defined by

$$\Delta u(\boldsymbol{x}_{i,j}) = \frac{u_{i-1,j} - 2u_{i,j} + u_{i+1,j}}{h_x^2} + \frac{u_{i,j-1} - 2u_{i,j} + u_{i,j+1}}{h_y^2} + O(h_x^2 + h_y^2).$$

Under the homogeneous Dirichlet boundary condition, matrix representation of the above discrete Laplace operator in one dimension (x-coordinate) can be written as

$$D_h^x = \frac{1}{h_x^2} \begin{bmatrix} -2 & 1 & & & \\ 1 & -2 & 1 & & \\ & \ddots & \ddots & \ddots & \\ & & 1 & -2 & 1 \\ & & & 1 & -2 \end{bmatrix}_{(N_x-1)\times(N_x-1)}, \tag{3.1}$$

i.e., $u_{xx} \approx D_h^x U$ since $u_{0,j} = u_{N_x,j} = 0$ for any $0 \leq j \leq N_y$. If the homogeneous Neumann (i.e., no-flux) boundary condition is used, then the one-dimensional Laplace operator D_h^x can be defined as

$$D_h^x = \frac{1}{h_x^2} \begin{bmatrix} -2 & 2 & & & \\ 1 & -2 & 1 & & \\ & \ddots & \ddots & \ddots & \\ & & 1 & -2 & 1 \\ & & & 2 & -2 \end{bmatrix}_{(N_x+1)\times(N_x+1)}, \tag{3.2}$$

in which $\frac{-2u_{0,j}+2u_{1,j}}{h_x^2}$ and $\frac{-2u_{N_x,j}+2u_{N_x-1,j}}{h_x^2}$ are used to approximate u_{xx} on the boundary nodes $x_{0,j}$ and $u_{N_x,j}$ respectively, which is equivalent to the ghost-point approach that sets $u_{-1,j} = u_{1,j}$ and $u_{N_x+1,j} = u_{N_x-1,j}$ according to $\frac{\partial u}{\partial \mathbf{n}} = 0$ and then applies the central differences. Mixed Dirichlet and Neumann boundary conditions can be treated by modifying the first and last row of D_h^x correspondingly. The discrete matrix D_h^y is defined in a similar way. With the help of Kronecker product, the discrete Laplace matrix in two dimensions is given by

$$D_h = I_{N_y-1} \otimes D_h^x + D_h^y \otimes I_{N_x-1} \tag{3.3}$$

where I_{N_y-1} and I_{N_x-1} are the identity matrices. Similarly, the corresponding matrix representation of the discrete Laplace operator in 3D can be represented by

$$D_h = I_{N_z-1} \otimes I_{N_y-1} \otimes D_h^x + I_{N_z-1} \otimes D_h^y \otimes I_{N_x-1} + D_h^z \otimes I_{N_z-1} \otimes I_{N_x-1}. \tag{3.4}$$

Let $\Phi_h(t)$ and $C_h(t)$ represent respectively the vectors consisting of the approximations of $\phi(\boldsymbol{x}, t)$ and $c(\boldsymbol{x}, t)$ on the mesh Ω_h. The spatially semi-discretized system with second-order accuracy for the pitting corrosion model is given by

$$\begin{cases} \dfrac{\mathrm{d}\Phi_h}{\mathrm{d}t} = -L(2A(c_{Le} - c_{Se})[C_h - h(\Phi_h)(c_{Se} - c_{Le}) - c_{Le}]h'(\Phi_h) + wg'(\Phi_h) - \alpha_\phi D_h \Phi_h) \\ \qquad := L\alpha_\phi D_h \Phi_h + F_1(\Phi_h, C_h), & (3.5) \\ \dfrac{\mathrm{d}C_h}{\mathrm{d}t} = MD_h\big(2A[C_h - h(\Phi_h)(c_{Se} - c_{Le}) - c_{Le}]\big) := F_2(\Phi_h, C_h), & (3.6) \end{cases}$$

where $\Phi_h(0)_{i,j} = \phi_0(\boldsymbol{x}_{i,j})$ and $C_h(0)_{i,j} = c_0(\boldsymbol{x}_{i,j})$ are the initial conditions. It should be noted that (3.5)–(3.6) is an ordinary differential equation (ODE) system now.

For more complicated metal microstructure morphology, the spatial discretization needs to be modified at some boundary or interface nodes in the finite difference method. For illustration, we consider a metal matrix that is otherwise homogeneous, except that it contains embedded particles/precipitates that do not corrode. In Figure 1, Cases I and II represent two typical situations of convex noncorroding particles represented by the yellow regions. At the nodes adjacent to the particle–matrix interface the homogeneous Neumann boundary (no-flux) condition needs to be enforced. We implement a simple first-order discretization of Δu at point $\boldsymbol{x}_{i,j}$ which is given by:

$$\Delta\phi(\boldsymbol{x}_{i,j}) \approx \frac{2\phi_{i-1,j} - 2\phi_{i,j}}{h_x^2} + \frac{\phi_{i,j-1} - 2\phi_{i,j} + \phi_{i,j+1}}{h_y^2}, \qquad \text{for Case I,} \tag{3.7}$$

$$\Delta\phi(\boldsymbol{x}_{i,j}) \approx \frac{2\phi_{i-1,j} - 2\phi_{i,j}}{h_x^2} + \frac{-2\phi_{i,j} + 2\phi_{i,j+1}}{h_y^2}, \qquad \text{for Case II.} \tag{3.8}$$

We use the above schemes to do the spatial approximation for the numerical experiment in subsection 4.5. Alternatively, the second order (or even higher-order) finite difference approximations of Δu may be defined at the interface nodes, as detailed in [57, 58].

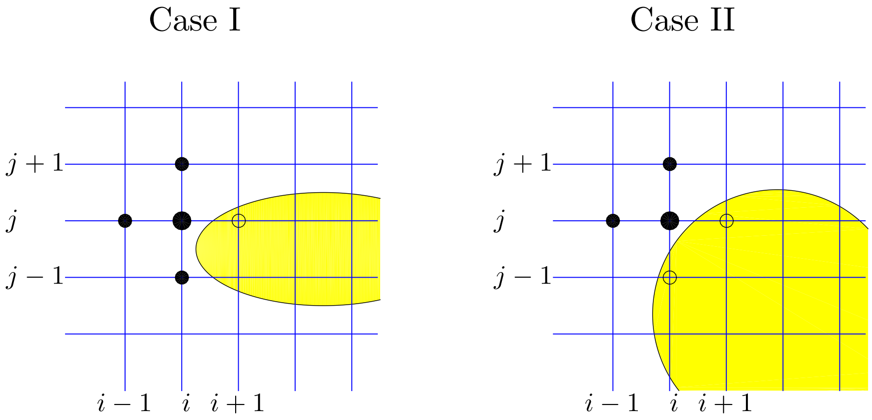

Figure 1: An illustration of the metal matrix with embedded noncorroding particles.

3.2. *Temporal integration*

We propose a decoupled second order accurate linear scheme for temporal discretization of the above ODE system (3.5)–(3.6). For simplicity, we assume a uniform time partition $\{t_n = n\tau\}_{n=0}^{N}$, where τ is the time step size; non-uniform temporal discretization can also be derived similarly with minor modifications of notations and formulas.

For the sake of clarity, we provide a brief introduction to the Rosenbrock–Euler exponential time integrator. We begin with the following ODE system

$$\frac{\mathrm{d}u(t)}{\mathrm{d}t} = F(u(t)), \quad t \in [0, t_N], \quad u(0) = u_0, \tag{3.9}$$

where $u \in \mathbb{R}^n$ represents the state vector and $F : \mathbb{R}^n \to \mathbb{R}^n$ is the vector field. By linearizing $F(u(t))$ at $u(t_n)$, we obtain

$$\frac{\mathrm{d}u(t)}{\mathrm{d}t} = J_n u(t) + [F(u(t)) - J_n u(t)] := J_n u(t) + G_n(u(t)), \qquad t \in [t_n, t_{n+1}], \tag{3.10}$$

where the Jacobian $J_n = \frac{\partial F(u)}{\partial u}|_{u(t_n)}$. The state vector $u(t_{n+1})$ at time t_{n+1} can be expressed in the integral form as:

$$u(t_{n+1}) = e^{\tau J_n} u(t_n) + \int_0^\tau e^{(\tau - s)J_n}\, G_n(u(t_n + s))\,\mathrm{d}s. \tag{3.11}$$

By taking $G_n(u(t_n + s)) \approx G_n(u(t_n))$ for $s \in [0, \tau]$, the Rosenbrock–Euler scheme is defined by

$$\begin{aligned} u_{n+1} &= e^{\tau J_n} u_n + \int_0^\tau e^{(\tau - s)J_n}\, G_n(u_n)\,\mathrm{d}s \\ &= e^{\tau J_n} u_n + \tau\varphi_1(\tau J_n) G_n(u_n)\,, \end{aligned} \tag{3.12}$$

where $\varphi_1(z) = (e^z - 1)/z$. The above scheme in (3.12) can be simplified as

$$u_{n+1} = u_n + \tau\varphi_1(\tau J_n)\, F(u_n) \tag{3.13}$$

Temporal error analysis shows that this is a second-order time integration method for the model ODE system (3.9); for more details the reader is referred to [19].

To overcome the high stiffness of the ODE system (3.5)–(3.6), we can apply the Rosenbrock–Euler integrator (3.13) directly to solve the coupled system. Thus, knowing $[\Phi_h^n, C_h^n]^T$, we can compute $(\Phi_h^{n+1}, C_h^{n+1})^T$ at the next time step as

$$\begin{bmatrix} \Phi_h^{n+1} \\ C_h^{n+1} \end{bmatrix} = \begin{bmatrix} \Phi_h^{n} \\ C_h^{n} \end{bmatrix} + \tau\varphi_1(\tau \boldsymbol{J}^n) \begin{bmatrix} L\alpha_\phi D_h\, \Phi_h^n + F_1(\Phi_h^n, C_h^n) \\ F_2(\Phi_h^n, C_h^n) \end{bmatrix} \tag{3.14}$$

with appropriate boundary conditions, where

$$\boldsymbol{J}^n = \begin{pmatrix} L\alpha_\phi D_h + \frac{\partial F_1}{\partial \Phi_h}(\Phi_h^n, C_h^n) & \frac{\partial F_1}{\partial C_h}(\Phi_h^n, C_h^n) \\ \frac{\partial F_2}{\partial \Phi_h}(\Phi_h^n, C_h^n) & \frac{\partial F_2}{\partial C_h}(\Phi_h^n, C_h^n) \end{pmatrix} \tag{3.15}$$

denotes the corresponding global Jacobian matrix at time t_n of the coupled system. However, the above approach results in a large $\boldsymbol{J}^n$ matrix. Because we need to perform matrix exponential and product calculations to evaluate $\exp(\tau \boldsymbol{J}^n)V$ (V is a certain vector) at each time step, this approach is quite expensive in practice, even with the Krylov subspace method [2] for large-scale sparse matrices. Instead of treating ϕ and c in a global way, an alternative approach is to decouple the system and solve the two variables ϕ and c separately.

The key idea of our scheme is to only apply the Rosenbrock–Euler integrator to (3.5) for computing Φ_h, due to its high stiffness, and apply low-cost semi-implicit schemes to (3.6) for computing C_h. By using a variable splitting approach, both Φ_h and C_h can be solved with larger time step size τ, which in turn improves the overall efficiency. We now apply this decouple numerical scheme to the phase field model for corrosive dissolution. We define the extrapolation

$$\widehat{C}_h^{n+1/2} = \frac{3}{2} C_h^n - \frac{1}{2} C_h^{n-1}, \tag{3.16}$$

and for $t \in [t_n, t_{n+1}]$, so that equation (3.5) can be approximated as

$$\frac{\mathrm{d}\Phi_h}{\mathrm{d}t} = L\,\alpha_\phi\, D_h \Phi_h + F_1(\Phi_h, \widehat{C}_h^{n+1/2}) := \boldsymbol{J}_\phi(\Phi_h^n, \widehat{C}_h^{n+1/2})\, \Phi_h + \boldsymbol{G}(\Phi_h, \widehat{C}_h^{n+1/2}), \tag{3.17}$$

where

$$\boldsymbol{J}_\phi(\Phi_h, C_h) = L\,\alpha_\phi\, D_h + \frac{\partial F_1}{\partial \Phi_h}(\Phi_h, C_h), \tag{3.18}$$

is the Jacobian matrix of the right hand side of (3.5) with respect to ϕ and

$$\boldsymbol{G}(\Phi_h, C_h) = F_1(\Phi_h, C_h) - \frac{\partial F_1}{\partial \Phi_h}(\Phi_h^n, C_h)\, \Phi_h. \tag{3.19}$$

Note that by definition $\frac{\partial F_1}{\partial \Phi_h}(\Phi_h, C_h)$ is a diagonal matrix. By combining the Rosenbrock–Euler and Crank–Nicolson schemes, a fully discrete, hybrid scheme for solving $(\Phi_h^{n+1}, C_h^{n+1})$ is obtained as: for $n = 1, 2, \cdots, N-1$,

$$\begin{cases} \Phi_h^{n+1} = \Phi^n + \tau\varphi_1(\tau \boldsymbol{J}_\phi(\Phi_h^n, \widehat{C}_h^{n+1/2}))\, (L\alpha_\phi D_h\, \Phi_h^n + F_1(\Phi_h^n, \widehat{C}_h^{n+1/2})), & (3.20) \\ \frac{C_h^{n+1} - C_h^n}{\tau} - AMD_h(C_h^{n+1} + C_h^n) = -2AMD_h\Big(h(\frac{\Phi_h^{n+1} + \Phi_h^n}{2})(c_{Se} - c_{Le}) + c_{Le}\Big). & (3.21) \end{cases}$$

As shown by local truncation error analysis presented in subsection 3.3, the above scheme (3.20)–(3.21) is second-order accurate in both time and space for homogeneous material systems.

In the above decoupled scheme, we can first solve Φ_h^{n+1} from (3.20), and then solve C_h^{n+1} by putting the computed Φ_h^{n+1} into (3.21). It is a linear scheme, so obviously a nonlinear iterative solver is not needed for solving (3.20) and (3.21). Because the proposed scheme applies a variable splitting approach, we only need to compute the matrix exponential $\exp(\tau \boldsymbol{J}_\phi)$ with the matrix $\boldsymbol{J}_\phi$, which is half the size of $\boldsymbol{J}^n$ in (3.14). Note that the computation of Φ_h^{n+1} dominates the computational expense, and the cost for solving C_h^{n+1} is almost negligible. To initiate the scheme (3.20)–(3.21), we consider a two-level temporal discretization scheme at the first time step t_1 as:

$$\begin{cases} \Phi_h^1 = \Phi_h^0 + \tau\varphi_1(\tau \boldsymbol{J}_\phi(\Phi_h^0, C_h^0))\,(L\alpha_\phi D_h\,\Phi_h^0 + F_1(\Phi_h^0, C_h^0)), & (3.22)\\ \dfrac{C_h^1 - C_h^0}{\tau} - 2AMD_hC_h^1 = -2AMD_h\Big(h(\Phi_h^1)(c_{Se} - c_{Le}) + c_{Le}\Big), & (3.23)\end{cases}$$

where Φ_h^0 and C_h^0 are defined as the initial conditions ϕ_0 and c_0, respectively. An alternative second-order scheme is to apply the BDF2 discretization instead of the Crank–Nicolson to (3.6). In the BDF2 scheme, one can solve for C_h^{n+1} as follows:

$$\frac{3C_h^{n+1} - 4C_h^n + C_h^{n-1}}{2\tau} - 2AMD_h\,C_h^{n+1} = -2AMD_h(h(\Phi_h^{n+1})(c_{Se} - c_{Le}) + c_{Le}). \tag{3.24}$$

3.3. Local truncation error analysis

Here we provide a local truncation error analysis for the proposed method to verify its second order convergence in both time and space. To this end, we assume the homogeneous Dirichlet boundary condition is imposed and the exact solution (ϕ, c) of the pitting corrosion system (2.11)-(2.12) has enough regularity for the error analysis.

We first need to show that the point-wise local truncation error of (3.20)–(3.21) for each time step $n \geq 1$ is $O(\tau^3 + \tau h^2)$. Taking the exact solution $(\phi(\boldsymbol{x}, t), c(\boldsymbol{x}, t))$ into (3.21), we can show that

$$\begin{aligned} &\vec{c}(t_{n+1}) - \vec{c}(t_n) - \tau AMD_h(\vec{c}(t_{n+1}) + \vec{c}(t_n)) \\ &\qquad = -2\tau AMD_h\left[h\left(\frac{\vec{\phi}(t_{n+1}) + \vec{\phi}(t_n)}{2}\right)(c_{Se} - c_{Le}) + c_{Le}\right] + O((\tau^3 + \tau h^2)\vec{1}), \end{aligned} \tag{3.25}$$

where $\vec{1} = (1, 1, \cdots, 1)^T$, $\vec{\phi}(t) = \{\phi(\boldsymbol{x}_{i,j}, t)\}$ and $\vec{c}(t) = \{c(\boldsymbol{x}_{i,j}, t)\}$ represent the vectors consisting of the values of ϕ and c, respectively, corresponding to the discretized domain Ω_h.

The local truncation error analysis for (3.20) needs more effort where the special nonlinear coupling of ϕ and c plays a key role. Taking the exact solution $(\phi(\boldsymbol{x}, t), c(\boldsymbol{x}, t))$ into the semi-discretized scheme (3.5) gives us

$$\frac{\mathrm{d}\vec{\phi}}{\mathrm{d}t} = L\alpha_\phi D_h\,\vec{\phi} + F_1(\vec{\phi}, \vec{\tilde{c}}(t_{n+1/2})) + O((\tau^2 + h^2)\vec{1}), \qquad t \in [t_n, t_{n+1}]. \tag{3.26}$$

and further

$$\begin{aligned} \frac{\mathrm{d}\vec{\phi}}{\mathrm{d}t} &= L\alpha_\phi D_h\,\vec{\phi} + F_1(\vec{\phi}(t_n), \vec{\tilde{c}}(t_{n+1/2})) + O((\tau^2 + h^2)\vec{1}) \\ &= \boldsymbol{J}_\phi(\vec{\phi}(t_n), \vec{\tilde{c}}(t_{n+1/2}))\,\vec{\phi} + \boldsymbol{G}(\vec{\phi}, \vec{\tilde{c}}(t_{n+1/2})) + O((\tau^2 + h^2)\vec{1}) \\ &= \boldsymbol{J}_\phi(\vec{\phi}(t_n), \vec{\tilde{c}}(t_{n+1/2}))\,\vec{\phi} + \boldsymbol{G}(\vec{\phi}_n, \vec{\tilde{c}}(t_{n+1/2})) + O((\tau^2 + h^2)\vec{1}), \end{aligned} \tag{3.27}$$

where $\boldsymbol{J}_\phi(\vec{\phi},\vec{c}) = L\alpha_\phi D_h + \frac{\partial F_1}{\partial \vec{\phi}}(\vec{\phi},\vec{c})$ and $\boldsymbol{G}(\vec{\phi},\vec{c}) = F_1(\vec{\phi},\vec{c}) - \frac{\partial F_1}{\partial \vec{\phi}}(\vec{\phi}_n,\vec{c})\,\vec{\phi}$. Note that the last equality comes from the fact that

$$F_1(\vec{\phi},\vec{c}(t_{n+1/2})) - F_1(\vec{\phi}_n,\vec{\hat{c}}(t_{n+1/2})) = \frac{\partial F_1}{\partial \vec{\phi}}(\vec{\phi}_n,\vec{\hat{c}}(t_{n+1/2}))\,(\vec{\phi}-\vec{\phi}_n) + O(\tau^2\vec{1}).$$

Then, it holds that

$$\begin{aligned}
\vec{\phi}(t_{n+1}) &= e^{\tau \boldsymbol{J}_\phi(\vec{\phi}(t_n),\vec{\hat{c}}(t_{n+1/2}))}\vec{\phi}(t_n) + \int_0^\tau e^{(\tau-s)\boldsymbol{J}_\phi(\vec{\phi}(t_n),\vec{\hat{c}}(t_{n+1/2}))}\boldsymbol{G}(\vec{\phi}(t_n),\vec{\hat{c}}(t_{n+1/2}))\\
&\quad + \int_0^\tau e^{(\tau-s)\boldsymbol{J}_\phi(\vec{\phi}(t_n),\vec{\hat{c}}(t_{n+1/2}))}O((\tau^2+h^2)\vec{1})\mathrm{d}s\\
&= \vec{\phi}(t_n) + \tau\varphi_1(\boldsymbol{J}_\phi(\vec{\phi}(t_n),\vec{\hat{c}}(t_{n+1/2})))(L\alpha_\phi D_h\,\vec{\phi}(t_n) + F_1(\vec{\phi}(t_n),\vec{\hat{c}}(t_{n+1/2})))\\
&\quad + \int_0^\tau e^{(\tau-s)\boldsymbol{J}_\phi(\vec{\phi}(t_n),\vec{\hat{c}}(t_{n+1/2}))}O((\tau^2+h^2)\vec{1})\mathrm{d}s
\end{aligned}$$

For the scaled discrete Laplace matrix $L\alpha_\phi D_h$, it holds that

$$\|e^{sL\alpha_\phi D_h}\|_\infty \leq 1, \qquad \forall\, s \geq 0,$$

according to Theorem 2 in [28]. Thus, for any $0 \leq s \leq \tau$, it holds

$$\begin{aligned}
\|e^{(\tau-s)\boldsymbol{J}_\phi(\vec{\phi}(t_n),\vec{\hat{c}}(t_{n+1/2}))}\|_\infty &= \left\|e^{(\tau-s)L\alpha_\phi D_h}e^{\frac{\partial F_1}{\partial \vec{\phi}}(\vec{\phi}(t_n),\vec{\hat{c}}(t_{n+1/2})}\right\|_\infty\\
&\leq \|e^{(\tau-s)L\alpha_\phi D_h}\|_\infty \left\|e^{\frac{\partial F_1}{\partial \vec{\phi}}(\vec{\phi}(t_n),\vec{\hat{c}}(t_{n+1/2})}\right\|_\infty\\
&\leq \left\|e^{\frac{\partial F_1}{\partial \vec{\phi}}(\vec{\phi}(t_n),\vec{\hat{c}}(t_{n+1/2})}\right\|_\infty\\
&\leq \text{Constant,}
\end{aligned} \tag{3.28}$$

where we have used the regularity of (ϕ, c) and the fact that $\frac{\partial F_1}{\partial \vec{\phi}}(\vec{\phi},\vec{c})$ is a diagonal matrix. With the bound (3.28), we obtain

$$\left\|\int_0^\tau e^{(\tau-s)\boldsymbol{J}_\phi(\vec{\phi}(t_n),\vec{\hat{c}}(t_{n+1/2}))}O((\tau^2+h^2)\vec{1})\ \mathrm{d}s\right\|_\infty = \tau\|O((\tau^2+h^2)\vec{1})\|_\infty = O(\tau^3+\tau h^2), \tag{3.29}$$

which gives us the local truncation error estimate for (3.20) as

$$\vec{\phi}(t_{n+1}) = \vec{\phi}(t_n) + \tau\varphi(\boldsymbol{J}_\phi(\vec{\phi}(t_n),\vec{\hat{c}}(t_{n+1/2})))(L\alpha_\phi D_h\,\vec{\phi}(t_n) + F_1(\vec{\phi}(t_n),\vec{\hat{c}}(t_{n+1/2}))) + O((\tau^3+\tau h^2)\vec{1}).$$

The formula (3.22)–(3.23) is applied only once (at the first step $n = 0$) for the purpose of startup, therefore it is easy to show in a similar way that their corresponding point-wise local truncation errors are $O(\tau^2 + \tau h^2)$. Overall, the final error is expected to be $O(\tau^2 + h^2)$ after time integration, that is, the scheme is second order accurate.

4. Numerical experiments

In this section, we present several numerical experiments to establish the viability of the proposed method (3.20)–(3.21) for the phase field model of corrosive dissolution. These numerical examples are adopted from [9, 32]. The package `Expokit` [44] based on the Krylov subspace method is used for computing the action of a matrix exponential on a vector. We use the `bicgstab` to solve for c. All numerical experiments are conducted on a Linux laptop with a quad-core Intel 2.5GHz Processor and 7.9GB Memory.

4.1. Numerical convergence test

In this example, we shall test the convergence rates of the proposed scheme using manufactured solutions. Here, we consider the following equation system

$$\begin{cases} \dfrac{\partial \phi}{\partial t} = \dfrac{c}{2+\cos(\pi x)} h'(\phi) + \Delta \phi, & x \in (0,1) \quad (4.1) \\ \dfrac{\partial c}{\partial t} = \Delta\big(c + h(\phi)\big) + r(x,t), & x \in (0,1) \quad (4.2) \end{cases}$$

where $h(\phi) = \phi^2$. The exact solutions are given by

$$\phi(x,t) = \cos(\pi x)\exp(2t^3), \qquad c(x,t) = (3t^2 + \frac{\pi^2}{2})(2 + \cos(\pi x)). \tag{4.3}$$

The initial conditions and the source function $r(x,t)$ are determined by the above exact solution (4.3). Homogeneous Neumann boundary condition is supplemented to the above problem (4.1)–(4.2). This manufactured problem is modified from the PFM for corrosion (2.11)–(2.12), where the essential nonlinear coupling between ϕ and c is preserved by the term $\frac{c}{2+\cos(\pi x)} h'(\phi)$. We set the terminal time $t_N = 0.5$.

To test the second-order temporal convergence, we solve (4.1)–(4.2) on a fixed spatial mesh with $N_x = 1024$ and gradually refine the time step sizes $\tau = 1/2^{4+j}$, for $j = 1, \ldots, 4$. The discrete L^2-norm errors of ϕ and c are reported in Table 2, which demonstrate that the scheme is second-order accurate in time. To test the spatial convergence rate, we fix the time step size $\tau = \frac{1}{1024}$ and gradually refine the spatial meshes with $N_x = 2^{4+j}$ for $j = 1, \ldots, 4$. We present the discrete L^2-norm errors of ϕ and c in Table 3 and observe that the scheme is second-order accurate in space for homogeneous domains.

Table 2: Discrete L^2-norm errors of the proposed scheme with gradually refined time step sizes on a fixed spatial mesh with $N_x = 1024$.

τ	$\|\phi^N - \Phi_h^N\|_{L^2}$	Order	$\|c^N - C_h^N\|_{L^2}$	Order
1/32	1.3952e-02	-	1.2535e-02	-
1/64	3.6904e-03	1.92	3.2767e-03	1.94
1/128	9.3286e-04	1.98	8.2848e-04	1.98
1/256	2.2382e-04	2.06	2.0239e-04	2.03

Table 3: Discrete L^2-norm errors of the proposed scheme on gradually refined spatial meshes with a fixed time step size $\tau = \frac{1}{1024}$.

h	$\|\phi^N - \Phi_h^N\|_{L^2}$	Order	$\|c^N - C_h^N\|_{L^2}$	Order
1/32	1.6712e-02	-	1.0669e-02	-
1/64	4.1337e-03	2.02	2.6126e-03	2.03
1/128	1.0183e-03	2.02	6.3930e-04	2.03
1/256	2.4306e-04	2.07	1.5079e-04	2.08

Table 4: The physical parameters of phase field model for corrosive dissolution.

Parameter	Physical interpretation	Value
σ	Interface energy	10 J/m^2
l	Interface thickness	5 μm
D	Diffusion coefficient	8.5×10^{-10} m^2/s
L	Interface kinetics coefficient	2 m^3/(Js)
A	Free energy density curvature	5.35×10^7 J/mol
$\bar{c}_{\text{solid}}$	Average concentration of metal	143 mol/L
$\bar{c}_{\text{sat}}$	Average saturation concentration	5.1 mol/L

4.2. Pencil electrode experiment

In this example, we use the proposed scheme to simulate the one-dimensional "pencil electrode experiment" conducted in [11]. The specimen is a 150 μm long stainless steel (304 SS) wire with diameter $d = 25$ μm mounted in an epoxy resin. Only the top end of the wire is exposed to the electrolyte solution, as shown in Figure 2. Therefore, we set the Dirichlet boundary condition $c = 0$ and $\phi = 0$ at the top, and $c = 1$ and $\phi = 1$ at the bottom boundary, whereas the homogeneous Neumann boundary condition is assigned along the length (cylindrical surface) of the wire. At the initial time $t = 0$, the whole domain Ω is in the uncorroded state, that is, $c = 1$ and $\phi = 1$. All model parameters are listed in Table 4, which are assumed from [32].

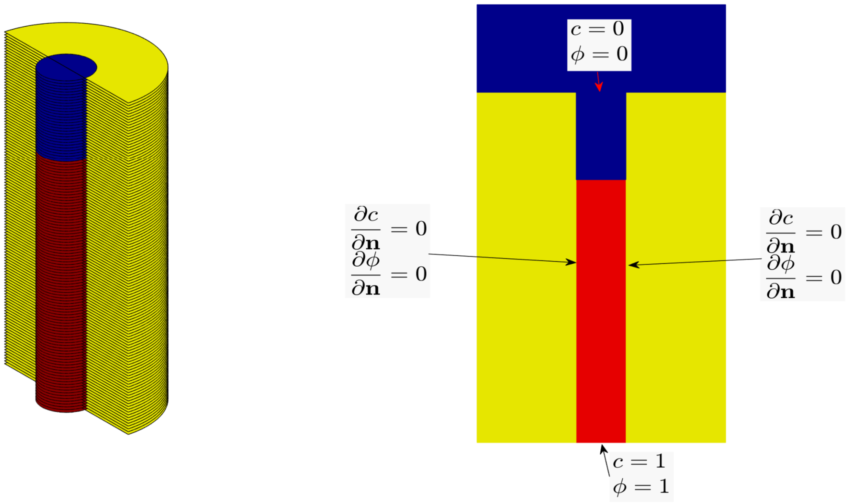

Figure 2: A schematic illustration of the pencil electrode experiment.

This example was solved in [32] using the finite element method to discretize in space together with an adaptive BDF2 scheme to discretize in time. The interface thickness parameter l is 5 μm. As remarked by Mai and co-workers in [32], accurate evaluation of the field variables (ϕ, c) requires that the mesh resolution be at least 1 μm in each direction near the interface. More importantly, an extremely small time step $\tau = 10^{-8}$ second was required initially to ensure convergence of the nonlinear solver and to alleviate oscillations in (ϕ, c) solutions. Herein, we use the proposed scheme to solve this example problem on a 25×150 uniform grid with a resolution of 1 μm throughout the domain. We find that the use of the time step size $\tau = 10^{-3}$ second is stable for the entire evolution process for our method, which is much larger than that of the conventional BDF type schemes. The proposed scheme uses a CPU time of 16205 seconds to arrive at $t = 225$ second. Figure 3 presents the numerical results of the material state ϕ and the concentration c at $t = 0$, 38, 152 and 225 seconds. We also plot the evolution of the pit depth ($\phi = 0.5$) in Figure 4, which agrees well with previous results obtained in [32, Section 3.1], the analytic solution in [42] and the experimental data in [11]. As expected during diffusion-controlled corrosion, the pit depth increases linearly with the square root of time.

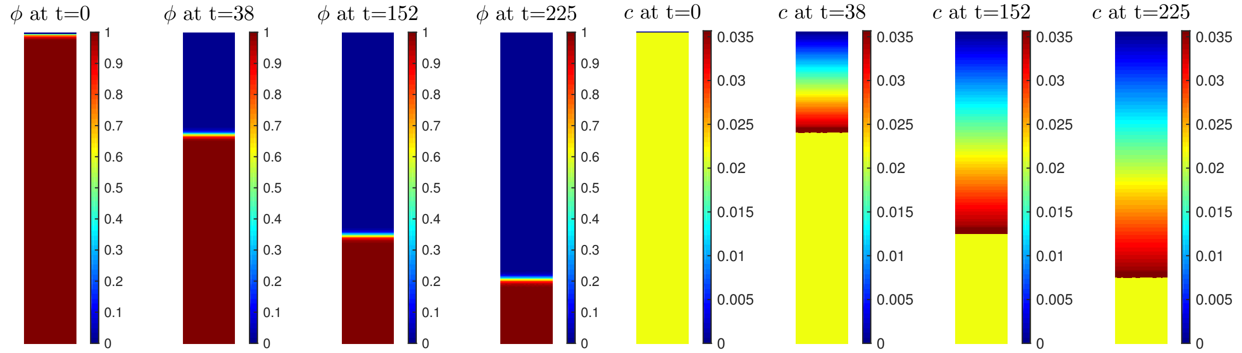

Figure 3: Simulated results by the proposed scheme with the time step size $\tau = 10^{-3}$ second and the spatial mesh resolution 1 μm for the pencil electrode test.

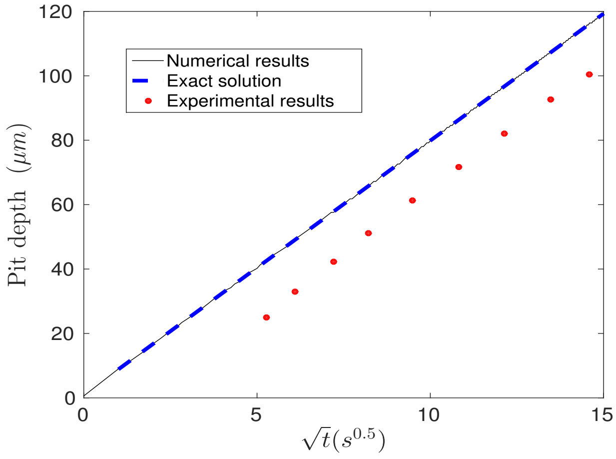

Figure 4: Simulated evolution of the pit depth is plotted against the data from the pencil electrode experiment in [11] and the exact analytical solution from [42].

It should be remarked that computational cost needed by the proposed scheme (3.20)–(3.21) could be significantly less than that by the scheme (3.14), which directly applies the Rosenbrock–Euler integrator to the whole ODE system (3.5)–(3.6). We observe that, when the terminal time is $t = 1$ second, the CPU time used by the proposed scheme is only 79.8 seconds, compared to 6,972 seconds by the scheme (3.14).

Next we investigate the performance of the proposed scheme (3.20)–(3.21) on finer meshes. When the spatial mesh is further refined, the discretized corrosion model becomes stiffer, which then requires even smaller time step sizes τ. At the same time, the total size of the ODE system is also getting scaled accordingly. When a uniform grid of 33×198 (resolution 0.75 μm) is used, we find that $\tau = 7.5\times10^{-4}$ second is stable for the proposed scheme which needs about a CPU time of 180.2 seconds to arrive at $t = 1$ seconds. If a 50×300 uniform grid (resolution 0.5 μm) is used, $\tau = 1.0\times10^{-4}$ second is needed for numerical stability and the proposed scheme costs a CPU time of 2,660 seconds to arrive at $t = 1$ second. Fortunately, we shall point out that the spatial resolution 1 μm is enough to capture the morphological evolution of corrosion interface, and with this resolution, the scheme (3.20)–(3.21) with the time step size $\tau = 1.0\times10^{-3}$ second is stable and efficient for the benchmark test (and all later examples).

4.3. Growth of an isolated pit

In this example, we use the proposed scheme to simulate the evolution of an isolated semi-circular pit growth, similar to the experiment conducted in [11]. We consider a specimen size of 400 μm × 200 μm. At the initial state ($t = 0$), we consider a semi-circular pit with diameter 16 μm situated at the center of the top edge, as shown in Figure 5. The homogeneous Dirichlet boundary condition is applied for both ϕ and c at the pit mouth region, while the homogeneous Neumann boundary condition is applied at the rest of the external domain boundary. All model parameters are listed in Table 4, which are assumed from [32].

We use the scheme described by (3.20)–(3.21) with the time step size $\tau = 10^{-3}$ second on a 400×200 uniform grid (resolution 1 μm in each direction) to do simulations. In this case, the dimension of the matrix in $\tau \boldsymbol{J}^n$ is 80610×80610, which is quite large. We observe that the proposed scheme (3.20)–(3.21) costs a CPU time of 1554.5 seconds to arrive at $t = 1$ second. The plots of the phase field variable ϕ at various times $t = 0$, 40, 100, 200, 400, 600 and 1000 seconds are provided in Figure 5. We also show the evolution of the pit depth versus time in Figure 6 by measuring the depth of the lowest point on the contour line corresponding to $\phi = 0.5$. Experiments by Ernst and Newman [11, Figure 8] show that the shape of an isolated corrosion pit remains circular, which qualitatively validates the results obtained in Figure 5. Currently, we do not have detailed experimental data in the literature to perform a quantitative calibration and validation of the phase field model with regards to pit shape evolution. The results of evolution of the morphology and pit depth exactly match with [32, Section 3.2]. However, compared to the BDF/BDF2 schemes used in [32], the proposed scheme is computationally more efficient because: (1) it allows the use of a larger time step size $\tau = 10^{-3}$ second even at initial times without loss of second-order accuracy in (ϕ, c) solutions; (2) the linear decoupled scheme does not require nonlinear (Newton) iterations.

4.4. Electropolishing of a metal surface

In this example, we use the proposed scheme to simulate the electropolishing process, which was studied previously in [32]. Electropolishing is widely used in the manufacturing industry as a surface treatment process to reduce the surface roughness of metallic materials [e.g., 26]. The metal with a rough surface is exposed to an appropriate electrolyte solution and a large anodic potential is applied to the metal to accelerate the corrosive dissolution process. In this case, the diffusion of metal ions in the solution environment limits the dissolution process at the corrosion interface (i.e., diffusion-controlled corrosion); consequently, the peaks in the surface roughness dissolve faster than the valleys, thus smoothing the surface. To simulate this process, here we consider a 400 μm × 200 μm rectangular domain with a rough surface at time $t = 0$, as shown in Figure 7. The homogeneous Dirichlet boundary condition is used on the top boundary, while the homogeneous Neumann boundary condition is used on the rest of the external domain boundary. For

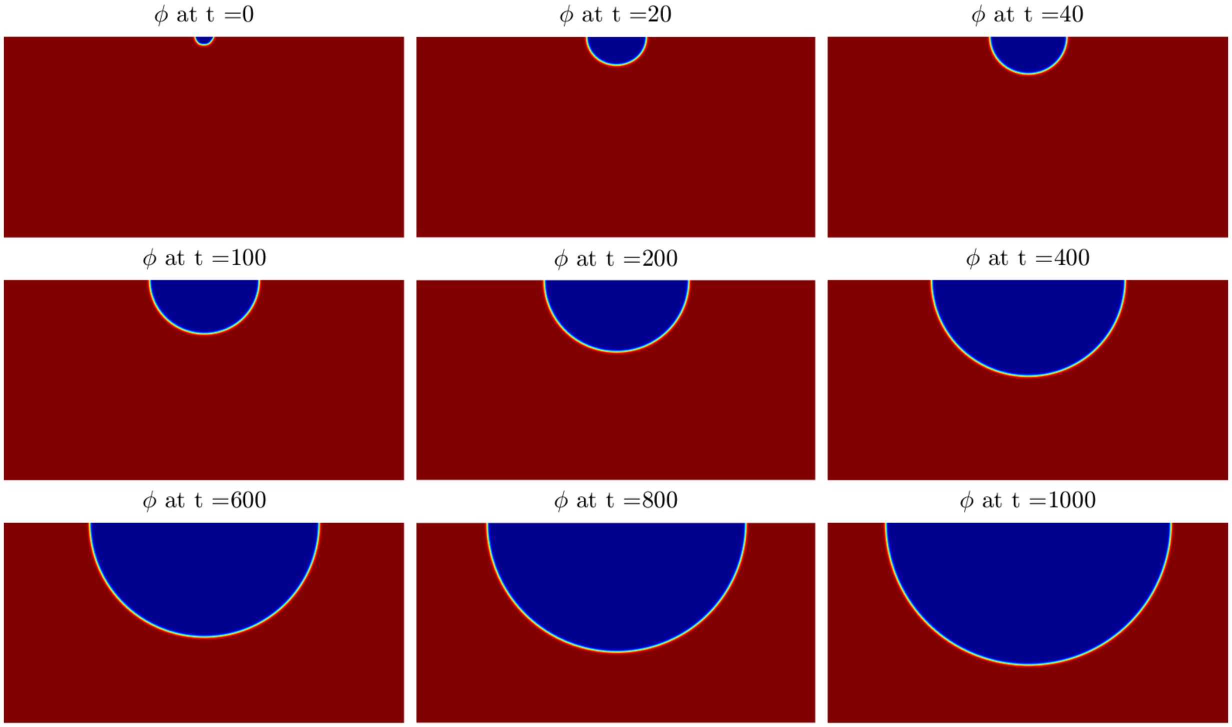

Figure 5: Simulated results by the proposed scheme with the time step size $\tau = 10^{-3}$ second on a uniform mesh with resolution 1 μm showing the growth of an isolated semi-circular pit.

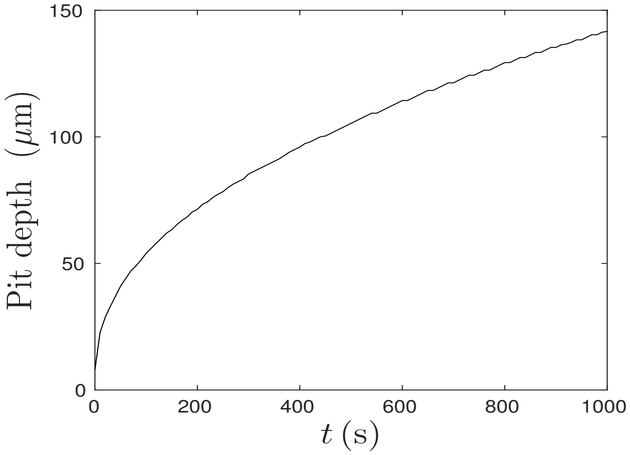

Figure 6: Simulated evolution of the pit depth with time during the growth of an isolated semi-circular pit. The pit depth is evaluated by measuring the depth of the lowest point on the contour line corresponding to $\phi = 0.5$.

illustration, we consider the model parameters in Table 4 calibrated for stainless steel 304 SS alloy. We use a uniform spatial mesh with resolution 1 μm in each direction and use the time step size $\tau = 10^{-3}$ second at all times. Numerical results of the material state ϕ at $t = 0, 1, 2, 3, 5, 10, 20, 100$ and 300 seconds are shown in Figure 7, which illustrates the transformation of an initially rough surface into a smoother surface due to diffusion-controlled corrosive dissolution. For this simulation, we observe that the proposed scheme (3.20)–(3.21) needs a CPU time of 1667.42 seconds to arrive at $t = 1$ second.

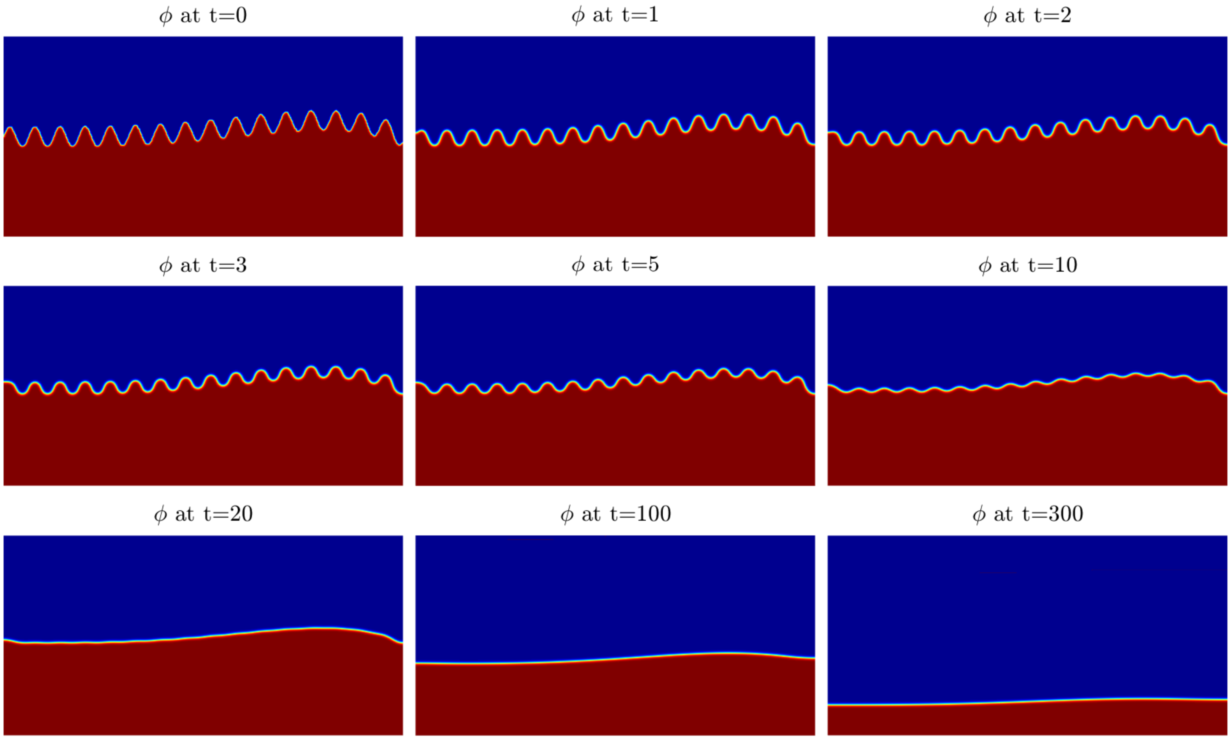

Figure 7: Simulated results by the proposed scheme with the time step size $\tau = 10^{-3}$ second on a uniform mesh with spatial resolution 1 μm, illustrating the electropolishing of a rough metal surface.

4.5. *Corrosion of an alloy with intermetallic particles*

In the final example, our aim is to demonstrate the ability of the proposed scheme to efficiently simulate the corrosive dissolution of an alloy matrix containing intermetallic particles or precipitates (IMPs) that are corrosion resistant. The presence of IMPs plays a crucial role in the susceptibility of stainless steel [5] and aluminum alloys [54]. In certain cases, the precipitates induce micro-galvanic corrosion processes because they have a different electrochemical potential than the surrounding alloy matrix [55]. Highly alloyed stainless steels and Ni-Fe-Cr alloys are particularly susceptible to localized corrosion (e.g., pitting) because the IMPs potentially reduce corrosion resistance of the surrounding matrix [52].

We consider a 200 μm × 200 μm square alloy matrix with distributions of noncorroding IMPs. At the initial state, we set a 10 μm pit on the top boundary, shown in Figure 8. The homogeneous Dirichlet boundary condition is used along the pit mouth on the top surface, while the homogeneous Neumann boundary condition is used on the rest of the external domain boundary and on the internal particle–matrix interfaces. For illustration, we consider the model parameters in Table 4 for the alloy matrix, which were calibrated for stainless steel 304 SS alloy. Due to the irregular shape of the ceramic particles, the morphological evolution of the pit is quite complicated even in the simple case of diffusion-controlled corrosion. We performed the same computations on a uniform 200×200, 250×250 mesh with a resolution of 1 μm and 0.8 μm, respectively. For these two grid resolutions, we find that the proposed scheme with the time step size $\tau = 10^{-3}$

second is stable. To arrive at $t = 1$ second, we observe that the CPU times of 840.58 seconds and 1356.09 seconds are needed, respectively. The snapshots of simulated results at $t = 1, 10, 40, 50, 100, 200, 300, 400$ and 500 seconds are shown in Figure 8, which demonstrate the robustness of the proposed scheme.

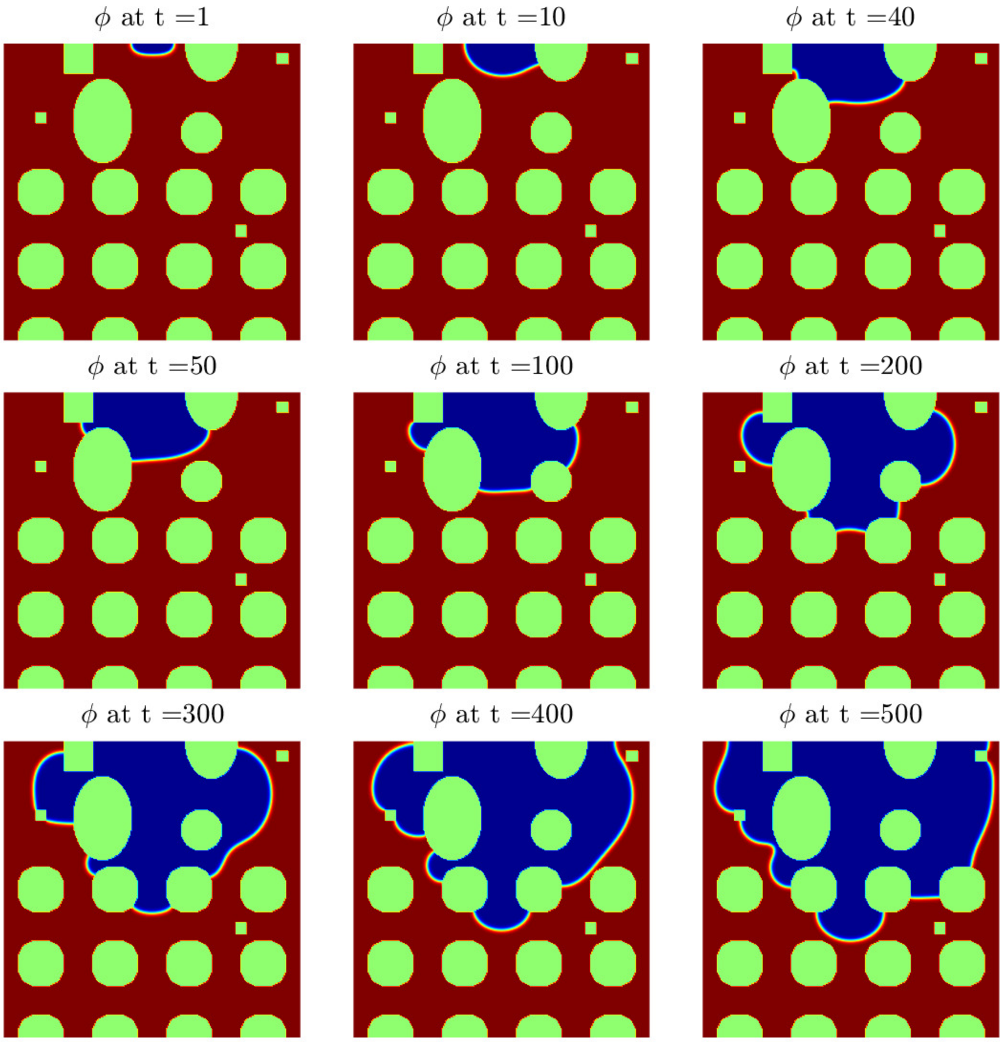

Figure 8: Simulated results by the proposed scheme with the time step size $\tau = 10^{-3}$ second on a uniform mesh with spatial resolution 1 μm for the corrosion of an alloy with intermetallic particles.

5. Conclusions

The phase field model for corrosive dissolution is highly nonlinear and computationally expensive to solve because of the strong numerical stiffness of the reaction-diffusion equation system. Consequently, implicit first/second order accurate backward difference formula (BDF/BDF2) schemes require very small time step sizes, as low as 10^{-8} second at initial times to ensure numerical stability or to avoid oscillations in the field variables. In this paper, we have developed an efficient decoupled linear numerical scheme, in which the equation for material corrosion/damage state ϕ is solved by the exponential time integrator, while the equation for c is solved by the conventional Crank–Nicolson scheme. We tested the accuracy, convergence and stability of the proposed numerical schemes by considering several numerical examples. We emphasize that the proposed scheme is stable with the time step size of 10^{-3} second at all times for the typical spatial resolution of 1 μm in all the example problems presented in this work. While we used central finite differences for spatial discretization, the proposed temporal discretization scheme and the decoupled approach can be easily extended to finite element and finite volume methods, where adaptive mesh refinement can be used to optimize the mesh for computational efficiency and to capture the domain or material microstructure geometries. Our future work will focus on implementing the proposed scheme in the finite element method to study stress corrosion cracking where it is important to account for the effects of elastic strain energy in the free energy functional. The proposed scheme is general enough to be applied to any phase field model encountering strong numerical stiffness, so we believe it would be relevant to the broader computational mathematics and material science community.

Acknowledgements

H. Gao's research is partially supported by National Natural Science Foundation of China under grants 11871234 and 11971010 and Hubei Key Laboratory of Engineering Modeling and Scientific Computing. L. Ju's research is partially supported by US National Science Foundation under grant DMS-1818438. H. Li's research is partially supported by National Natural Science Foundation of China under grants 11401350 and 11471196 and Natural Science Foundation of Shandong Province under grant ZR2019BA002.

References

[1] A. Abubakar, S. Akhtar and A.F.M. Arif, Phase field modeling of V_2O_5 hot corrosion kinetics in thermal barrier coatings, *Comput. Mater. Sci.*, 99(2015), pp. 105–116.

[2] E. Allopoulos and Y. Saad, Efficient solution of parabolic equations by Krylov approximation methods, *SIAM J. Sci. Stat. Comput.*, 13(1992), pp. 1236–1264.

[3] A. Al-Mohy and N. Higham, Computing the action of the matrix exponential, with an application to exponential integrators, *SIAM J. Sci. Comput.*, 33(2011), pp. 488–511.

[4] W. Boettinger, J. Warren, C. Beckermann and A. Karma, Phase-field simulation of solidification, *Annu. Rev. Mater. Res.*, 32(2002), pp. 163–194.

[5] K.W. Chan and S.C. Tjong, Effect of secondary phase precipitation on the corrosion behaviour of duplex stainless steels, *Materials*, 7(2014), pp. 5268–5304.

[6] L. Chen, Phase-field models for microstructure evolution, *Annu. Rev. Mater. Res.*, 32(2002), pp. 113–140.

[7] Z. Chen and F. Bobaru, Peridynamic modeling of pitting corrosion damage, *J. Mech. Phys. Solids*, 78(2015), pp. 352–381.

[8] Z.G. Chen, G.F. Zhang and F. Bobaru, The influence of passive film damage on pitting corrosion, *J. Electrochem. Soc.*, 163(2016), pp. C19–C24.

[9] R. Duddu, Numerical modeling of corrosion pit propagation using the combined extended finite element and level set method, *Comput. Mech.*, 54(2014), pp. 613–627.

[10] R. Duddu, N. Kota and S.M. Qidwai, An extended finite element method based approach for modeling crevice and pitting corrosion, *J. Appl. Mech.*, 83(2016), pp. 081003.

[11] P. Ernst and R. Newman, Pit growth studies in stainless steel foils. I. Introduction and pit growth kinetics, *Corros. Sci.*, 44(2002), pp. 927–941.

[12] G.S. Frankel and N. Sridhar, Understanding localized corrosion, *Mater. Today*, 11(2008), pp. 38–44.

[13] H. Gao and W. Sun, An efficient fully linearized semi-implicit Galerkin-mixed FEM for the dynamical Ginzburg–Landau equations of superconductivity, *J. Comput. Phys.*, 294(2015), pp. 329–345.

[14] S. Gaudreault and J. Pudykiewicz, An efficient exponential time integration method for the numerical solution of the shallow water equations on the sphere, *J. Comput. Phys.*, 322(2016), pp. 827–848.

[15] S. Gaudreault, G. Rainwater and M. Tokman, KIOPS: A fast adaptive Krylov subspace solver for exponential integrators, *J. Comput. Phys.*, 372(2018), pp. 236–255.

[16] N. Higham and A. Al-Mohy, Computing matrix functions, *Acta Numerica*, 19(2010), pp. 159–208.

[17] M. Hochbruck and C. Lubich, On Krylov subspace approximations to the matrix exponential operator, *SIAM J. Numer. Anal.*, 34(1997), pp. 1911–1925.

[18] M. Hochbruck, C. Lubich and H. Selhofer, Exponential integrators for large systems of differential equations, *SIAM J. Sci. Comput.*, 19(1998), pp. 1552–1574.

[19] M. Hochbruck and A. Ostermann, Exponential integrators, *Acta Numerica*, 19(2010), pp. 209–286.

[20] M. Hochbruck, A. Ostermann, and J. Schweitzer, Exponential Rosenbrock-type methods, *SIAM J. Numer. Anal.*, 47(2009), pp. 786–803.

[21] D. W. Hoeppner and A. M. H Taylor, AVT-140 Corrosion Fatigue and Environmentally Assisted Cracking in Aging Military Vehicles, chapter 13, *Modelling Pitting Corrosion Fatigue: Pit Growth and Pit/Crack Transition Issues*, NATO, RTO, NATO, France, 2011.

[22] L. Ju, J. Zhang and Q. Du, Fast and accurate algorithms for simulating coarsening dynamics of Cahn-Hilliard equations, *Comput. Mater. Sci.*, 108(2015), pp. 272–282.

[23] L. Ju and Z. Wang, Exponential time differencing gauge method for incompressible viscous flows, *Commun. Comput. Phys.*, 22(2017), pp. 517–541.

[24] A. Karma and W. Rappel, Phase-field method for computationally efficient modeling of solidification with arbitrary interface kinetics, *Phys. Rev. E*, 53(1996), pp. R3017.

[25] S. Kim, W. Kim and T. Suzuki, Phase-field model for binary alloys, *Physical Review E*, 60(1999), pp. 7186.

[26] D. Landolt, P. Chauvy and O Zinger, Electrochemical micromachining, polishing and surface structuring of metals: fundamental aspects and new developments, *Electrochim. Acta*, 48(2003), pp. 3185–3201.

[27] N. Laycok and S. White, Computer simulation of single pit propagation in stainless steel under potentiostatic control, *J. Electrochem. Soc.*, 148(2001), pp. B264–B275.

[28] A. Lazer, Characteristic exponents and diagonally dominant linear differential systems, *J. Math. Anal. Appl.*, 35(1971), pp. 215–229.

[29] S. Li, L. Luo, Z. Wang and L. Ju, An exponential time-integrator scheme for steady and unsteady inviscid flows, *J. Comput. Phys.*, 365(2018), pp. 206–225

[30] D.D. Macdonald and G.R. Engelhardt, 2.39 Predictive Modeling of Corrosion, in: *T.J.A. Richardson, B.R.A. Cottis, R. Lindsay, S. Lyon, D.J.D. Scantlebury, H. Stott, et al. (Eds.), Shreirs Corrosion, 4th ed.*, Elsevier B.V., 2010. pp. 1630–1679.

[31] D. Macdonald and M. Urquidi-Macdonald, Corrosion damage function-interface between corrosion science and engineering, *Corrosion*, 48(1992), pp. 354–367.

[32] W. Mai, S. Soghrati and R. Buchheit, A phase field model for simulating the pitting corrosion, *Corros. Sci.*, 110(2016), pp. 157–166.

[33] W. Mai and S. Soghrati, A phase field model for simulating the stress corrosion cracking initiated from pits, *Corros. Sci.*, 125(2017), pp. 87–98.

[34] W. Mai and S. Soghrati, New phase field model for simulating galvanic and pitting corrosion processes, *Electrochim. Acta*, 260(2018), pp. 290–304.

[35] N. Moelans, B. Blanpain and P. Wollants, An introduction to phase-field modeling of microstructure evolution, *Calphad*, 32(2008), pp. 268–294.

[36] A. Nauts and R. Wyatt, New approach to many-state quantum dynamics: The recursive-residue-generation method, *Phys. Rev. Lett.*, 51(1983), pp. 2238–2241.

[37] S. Nesic, M. Nordsveen, N. Maxwell and M. Vrhovac, Probabilistic modelling of CO_2 corrosion laboratory data using neural networks, *Corros. Sci.*, 43(2001), pp. 1373–1392.

[38] T. Park and J. Light, Unitary quantum time evolution by iterative Lanczos reduction, *J. Chem. Phys.*, 85(1986), pp. 5870–5876.

[39] S. Pfeifer, O. Wodo, B. Ganapathysubramanian, An optimization approach to identify processing pathways for achieving tailored thin film morphologies, *Comput. Mater. Sci.*, 143(2018), pp. 486–496.

[40] R.M. Pidaparti, L. Fang and M.J. Palakal, Computational simulation of multi-pit corrosion process in materials, *Comp. Mat. Sci.*, 41(2008), pp. 255–265.

[41] S. Sarkar, J.E. Warner and W. Aquino, A numerical framework for the modeling of corrosive dissolution, *Corros. Sci.*, 65(2012), pp. 502–511.

[42] S. Scheiner and C. Hellmich, Stable pitting corrosion of stainless steel as diffusion-controlled dissolution process with a sharp moving electrode boundary, *Corros. Sci.*, 49(2007) pp. 319–346.

[43] A. Sedriks, *Corrosion of Stainless Steel, 2nd ed.*, John Wiley and Sons, Inc, New York, NY, United States, 1996.

[44] R. Sidje, Expokit: A software package for computing matrix exponentials, *ACM Trans. Math. Software*, 24(1998), pp. 130–156.

[45] W. Sun, L. Wang, T. Wu and G. Liu, An arbitrary Lagrangian–Eulerian model for modelling the time-dependent evolution of crevice corrosion, *Corros. Sci.*, 78(2014), pp. 233–243.

[46] A. Tambue, I. Berre and J. Nordbotten, Efficient simulation of geothermal processes in heterogeneous porous media based on the exponential Rosenbrock–Euler and Rosenbrock-type methods, *Adv. Water Resour.*, 53(2013), pp. 250–262.

[47] S.K. Thamida, Modeling and simulation of galvanic corrosion pit as a moving boundary problem, *Comput. Mater. Sci.*, 65(2012), pp. 269–275.

[48] A. Turnbull, D.A. Horner and B.J. Connolly, Challenges in modeling the evolution of stress corrosion cracks from pits, *Eng. Fract. Mech.*, 76(2009), pp. 633–640.

[49] H. Vo and R. Sidje, Approximating the large sparse matrix exponential using incomplete orthogonalization and Krylov subspaces of variable dimension, *Numer. Linear Algebra Appl.*, 24(2017), pp. e2090.

[50] J. Warren and W. Boettinger, Prediction of dendritic growth and microsegregation patterns in a binary alloy using the phase-field method, *Acta Metall. Mater.*, 43(1995), pp. 689–703.

[51] A. Wheeler, B. Murray and R. Schaefer, Computation of dendrites using a phase field model, *Physica D*, 66(1993), pp. 243–262.

[52] M.E. Wilms, V.J. Gadgil, J.M. Krougman and F.P. Ijsseling, The effect of σ-phase precipitation at 800 °C on the corrosion resistance in sea-water of a high alloyed duplex stainless steel, *Corros. Sci.*, 36(1994), pp. 871–881.

[53] J. Xiao and S. Chaudhuri, Predictive modeling of localized corrosion: An application to aluminum alloys, *Electrochim. Acta*, 56(2011), pp. 5630–5641.

[54] K.A. Yasakau, M.L. Zheludkevich, S.V. Lamaka and M.G.S. Ferreira, Role of intermetallic phases in localized corrosion of AA5083, *Electrochim. Acta*, 52(2007), pp. 7651–7659.

[55] L. Yin, Y. Jin, C. Leygraf, N. Birbilis and J. Pan, Numerical simulation of micro-galvanic corrosion in Al alloys: effect of geometric factors, *J. Electrochem. Soc.*, 164(2017), pp. C75–C84.

[56] J. Zhang, C. Zhou, Y. Wang, L. Ju, Q. Du, X. Chi, D. Xu, D. Chen, Y. Liu and Z. Liu, Extreme-scale phase field simulations of coarsening dynamics on the Sunway TaihuLight supercomputer, *Proc. Inter. Conf. High Perf. Comput. Net. Storage Anal.* (2016), Article #4, Salt Lake City, UT, USA.

[57] S. Zhao, A fourth order finite difference method for waveguides with curved perfectly conducting boundaries, *Comput. Methods Appl. Mech. Engrg.*, 199(2010), pp. 2655–2662.

[58] S. Zhao, High order matched interface and boundary methods for the Helmholtz equation in media with arbitrarily curved interfaces, *J. Comput. Phys.*, 229(2010), pp. 3155–3170.